nature materials

LETTERS

PUBLISHED ONLINE: 13 JULY 2015 | DOI: 10.1038/NMAT4356

Resonant internal quantum transitions and femtosecond radiative decay of excitons in monolayer WSe_2

C. Poellmann[1], P. Steinleitner[1], U. Leierseder[1], P. Nagler[1], G. Plechinger[1], M. Porer[1], R. Bratschitsch[2], C. Schüller[1], T. Korn[1] and R. Huber[1]*

Atomically thin two-dimensional crystals have revolutionized materials science[1–3]. In particular, monolayer transition metal dichalcogenides promise novel optoelectronic applications, owing to their direct energy gaps in the optical range[4–9]. Their electronic and optical properties are dominated by Coulomb-bound electron–hole pairs called excitons[10–18], whose unusual internal structure[13], symmetry[15–17], many-body effects[18] and dynamics have been vividly discussed. Here we report the first direct experimental access to all 1*s* A excitons, regardless of momentum—inside and outside the radiative cone—in single-layer WSe_2. Phase-locked mid-infrared pulses reveal the internal orbital 1*s*–2*p* resonance, which is highly sensitive to the shape of the excitonic envelope functions and provides accurate transition energies, oscillator strengths, densities and linewidths. Remarkably, the observed decay dynamics indicates an ultrafast radiative annihilation of small-momentum excitons within 150 fs, whereas Auger recombination prevails for optically dark states. The results provide a comprehensive view of excitons and introduce a new degree of freedom for quantum control, optoelectronics and valleytronics of dichalcogenide monolayers[19–24].

Excitons emerge when photons promote electrons from the valence to the conduction band of a semiconductor. Each hole left behind can bind with an electron by Coulomb attraction. Like atoms, excitons are described by their centre-of-mass momentum, K, and discrete quantum numbers characterizing the relative electron–hole motion (Fig. 1a). In inorganic bulk semiconductors, typical binding energies amount to a few meV, owing to the small effective mass and dielectric screening. In monolayer transition metal dichalcogenides (TMDCs), such as MoS_2, $MoSe_2$, WS_2 or WSe_2, however, the two-dimensional electron confinement and suppressed screening leads to exotic, non-hydrogenic excitons with binding energies in excess of 0.2 eV (refs 10–17,25). Because these bound states remain stable at room temperature and dominate many optical and electronic properties of monolayer TMDCs, a detailed microscopic understanding is indispensable for prospective applications of TMDCs.

Spectroscopy with visible light probing electronic transitions across the direct energy gap, E_g, has provided key insight into the energy levels of bound states[2,11,13,14]. For instance, radiative recombination of bound electron–hole pairs causes photoluminescence (PL; refs 4–7) at a photon energy that is reduced with respect to E_g by the exciton binding energy. Furthermore, the small exciton Bohr radius leads to anomalously strong interband absorption[11–13,16,17,26]. Even excited and charged exciton states, called trions, are imprinted on interband spectra[2,10,14,15,22,25,27]. Yet, the negligible photon momentum restricts optical transitions to creating or annihilating excitons with $K \approx 0$ (Fig. 1a, blue vertical arrow). As a result of scattering, the majority of excitons can assume finite momenta, making them optically dark. Furthermore, interband excitation probes the envelope functions of bound electron–hole pairs only at vanishing electron–hole distance (Supplementary Equation 1) and evaluating interband dipole moments requires sophisticated band structure calculations[14]. Extracting quantitative information about densities, many-body interactions and ultrafast dynamics has, therefore, remained challenging.

Here we investigate a new class of quantum excitations in WSe_2: Internal transitions connecting different orbital states of bound electron–hole pairs[28,29] (see Fig. 1a, red arrows) by absorption of mid-infrared photons. This approach represents the first direct, destruction-free access to optically bright and dark 1*s* excitons of arbitrary momenta in a monolayer. The mid-infrared absorption coefficient depends sensitively on the spatial profile of the exciton's envelope function, but remains independent of interband dipole moments (Supplementary Equation 2). It allows us to establish a detailed picture of excitons in a monolayer TMDC, including absolute values for 1*s*–2*p* transition energies, oscillator strengths, particle densities, many-body interactions and ultrafast dynamics. Importantly, the giant interband dipole moment[26] leads to an extremely efficient radiative decay of excitons at $K \approx 0$.

Our WSe_2 samples are manufactured by mechanical exfoliation and transfer onto a CVD diamond window using a recently developed deterministic process[30]. Single-layer flakes with lateral dimensions above 70 μm are identified by optical microscopy (Fig. 1b) and PL mapping (Fig. 1c). The corresponding room-temperature PL spectrum (Fig. 1d, blue solid curve) features a peak wavelength of 750 nm, a width of 20 nm (FWHM) and a Stokes shift of 6 nm with respect to the absorption maximum (Supplementary Fig. 1), characteristic of the 1*s* state of the A exciton[7]. To explore the dynamics of these quasiparticles, we selectively inject excitons at $K = 0$ with a 90-fs laser pulse centred at $\lambda_c = 742$ nm (Fig. 1d, blue dashed curve). After a variable delay time t_{PP}, the low-energy dielectric response is probed by a phase-locked mid-infrared pulse (Fig. 1a), whose complete waveform is mapped out electro-optically[29] (see Methods) as a function of the recording time, t_{EOS}. Figure 1e shows the mid-infrared field transient transmitted through the unexcited sample, E_{ref} (black curve), and its pump-induced change, ΔE (red curve), recorded at a fixed delay time

[1]Department of Physics, University of Regensburg, D-93040 Regensburg, Germany. [2]Institute of Physics, University of Münster, D-48149 Münster, Germany. *e-mail: rupert.huber@ur.de

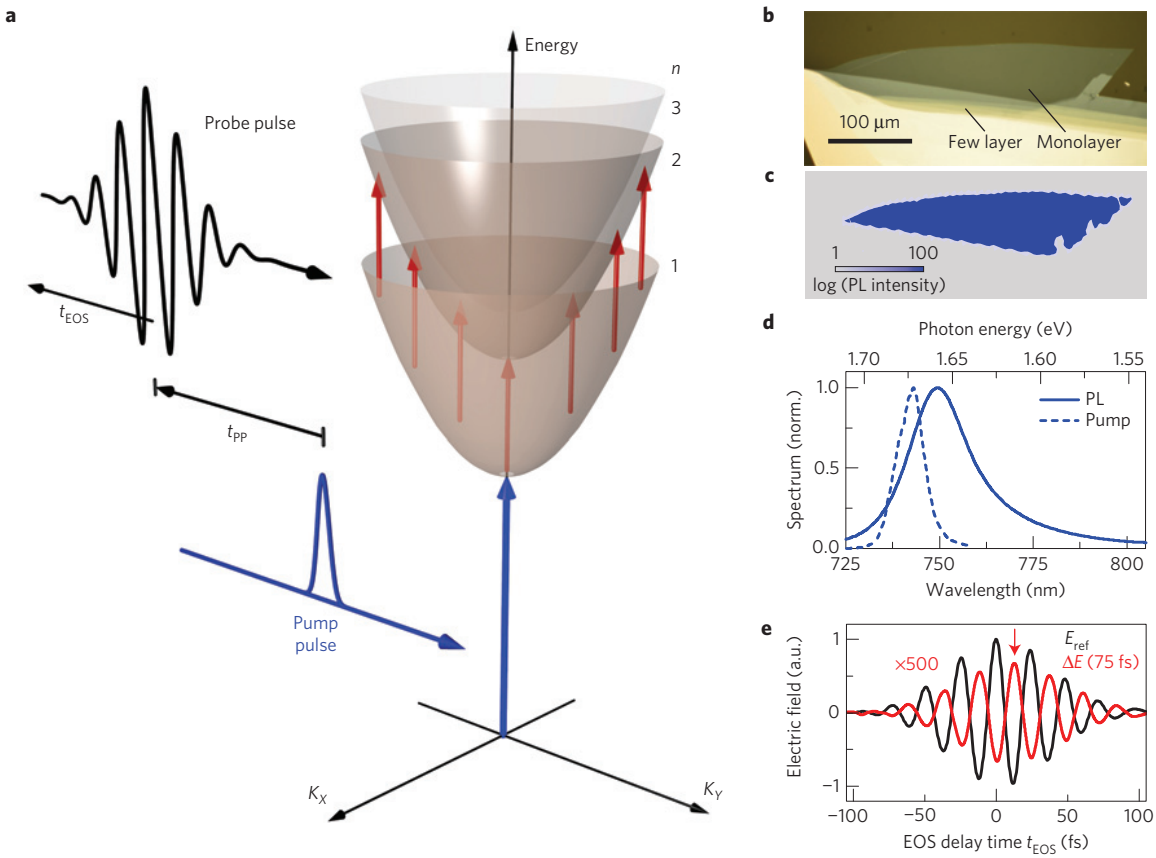

Figure 1 | Intra- and interband spectroscopy of single-layer WSe_2. a, Schematic dispersion (amber paraboloids) of excitons with different principal quantum numbers n, as a function of the centre-of-mass momentum $K=\sqrt{K_X^2+K_Y^2}$. In the time-resolved pump–probe experiment, 1s A excitons are resonantly generated at $K=0$ by a 90-fs near-infrared pump pulse (blue) while a mid-infrared transient (black waveform) delayed by t_{PP} probes the internal 1s–2p transition (red arrows) of all pre-existing excitons, irrespective of K. The oscillating carrier waveform of the probe pulse is directly mapped out as a function of the delay time t_{EOS}, by ultrabroadband electro-optic sampling. **b**,**c**, Optical microscopy image (**b**) and PL intensity map (**c**) of an exfoliated WSe_2 monolayer on a viscoelastic substrate before the transfer onto the diamond window (**b**) and thereafter (**c**). **d**, Measured photoluminescence spectrum (blue solid line) of the monolayer sample excited by a continuous-wave laser at a wavelength of 532 nm. Dashed blue line: Spectrum of the femtosecond pulse used in the pump–probe experiment. **e**, Waveform of the probe pulse E_{ref} (black curve) transmitted through the unexcited WSe_2 monolayer and pump-induced change ΔE (red curve, scaled up by a factor of 500) at $t_{PP}=75$ fs after resonant injection of 1s excitons. The red arrow indicates the maximum of $\Delta E(t_{EOS})$. All experiments are performed at room temperature.

$t_{PP}=75$ fs. ΔE roughly traces the reference pulse with a phase offset of π, indicating that the presence of 1*s* excitons reduces the amplitude of the transmitted probe field in the single-layer crystal.

The field-resolved time-domain data allow us to retrieve the full dielectric response of the excited sample[29], characterized by the real parts of the optical conductivity $\Delta\sigma_1$ (Fig. 2a) and the dielectric function $\Delta\varepsilon_1$ (Fig. 2b). $\Delta\sigma_1$, which is proportional to the mid-infrared absorption coefficient, exhibits a broad maximum whereas $\Delta\varepsilon_1$ follows a dispersive shape with a zero crossing at a photon energy of 162 meV. These spectra are in stark contrast to the Drude-like response of free electron–hole pairs observed after non-resonant above-bandgap excitation (Supplementary Figs 2 and 3b,c) and prove the existence of a new mid-infrared excitonic quantum transition in monolayer TMDCs. The resonance energy is compatible with the 1*s*–2*p* orbital exciton resonance extracted from recent interband spectroscopy[25] (see Supplementary Section 6). Figure 2c–f shows the pump-induced infrared response at $t_{PP}=275$ fs and 1.6 ps, respectively. Although the qualitative resonance features are similar to Fig. 2a and b, both the amplitude of $\Delta\sigma_1$ (Fig. 2c,e) and the slope of $\Delta\varepsilon_1$ (Fig. 2d,f) are reduced and the resonance slightly narrows and blueshifts with increasing t_{PP}.

For a quantitative analysis we describe the Wannier excitons in single-layer WSe_2 with a two-dimensional hydrogen model (see Supplementary Section 5) including nonlocal dielectric screening[13,15]. The latter renders the interaction potential non-Coulombic (Fig. 2h) and increases the 1*s* Bohr radius from 5 to 8.3 Å (Fig. 2g). Within this framework, we compute an energy separation between the 1*s* and 2*p* states of ∼170 meV (Fig. 2h), in good agreement with the resonance positions observed in our experiment. The oscillator strength of the corresponding internal resonance of a single electron–hole pair is found to be $f_{1s-2p}=0.32$ (Supplementary Equation 13). To simultaneously fit the experimental data $\Delta\sigma_1$ and $\Delta\varepsilon_1$, we keep the calculated value of f_{1s-2p} fixed, introduce a Lorentzian broadening of the 1*s*–2*p* oscillator and use the linewidth Δ, the 1*s* exciton density n_X and the exact resonance energy E_{res} as adjustable parameters (see shaded curves in Fig. 2a–f).

For $t_{PP}=75$ fs and 275 fs (Fig. 2a–d), the model perfectly describes both response functions with $E_{res}=162$ meV and 179 meV, respectively. Moreover, the 1*s* exciton density n_X obtained at $t_{PP}=75$ fs matches quantitatively with the density of absorbed pump photons of $n_a=(2.8\pm0.4)\times10^{12}$ cm^{-2} (see Supplementary Section 2). Neglecting nonlocal screening would reduce f_{1s-2p} by a factor of five and yield an unphysically large fitting parameter n_X. These observations confirm that our assignment of the infrared response to the 1*s*–2*p* transition is correct, the optical pump

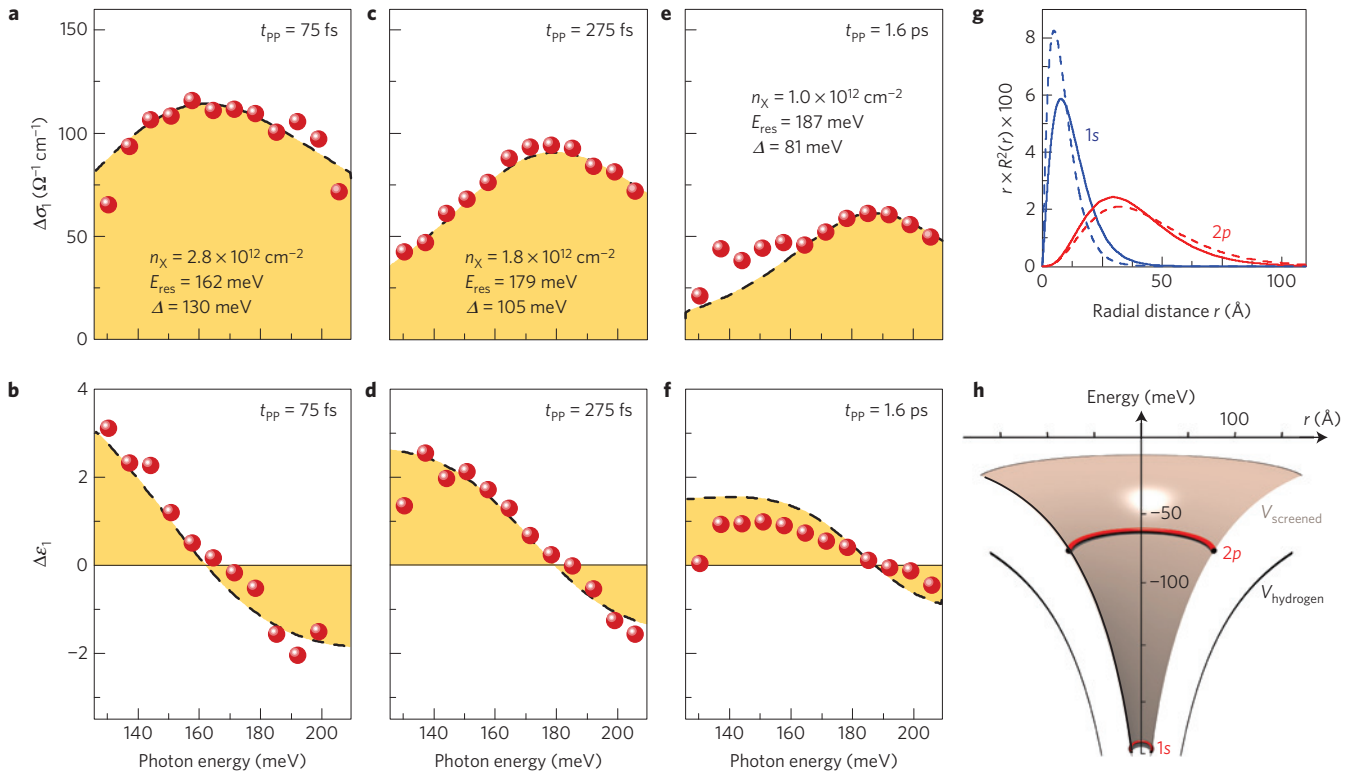

Figure 2 | Time-resolved response of the intra-excitonic 1s–2p transition. a,**c**,**e**, Real part of the pump-induced mid-infrared conductivity $\Delta\sigma_1(\hbar\omega)$ of photoexcited monolayer WSe_2, as a function of the photon energy, $\hbar\omega$, for three different delay times t_{PP} (pump fluence, $\Phi = 16\ \mu J\ cm^{-2}$). **b**,**d**,**f**, Corresponding real part of the dielectric function, $\Delta\varepsilon_1(\hbar\omega)$. Red spheres: Experimental data. Black dashed curve: Two-dimensional Wannier exciton model simultaneously fitting $\Delta\sigma_1$ and $\Delta\varepsilon_1$. The adapted parameters of 1s exciton density n_X, transition energy E_{res}, and linewidth Δ, are given in **a**,**c** and **e**. **g**, Radial electron distribution of the 1s (blue) and the 2p (red) exciton for a two-dimensional model assuming a locally screened (dashed) and a nonlocally screened (solid) potential[13], as a function of the radial distance r. **h**, Interaction potential $V_{screened}$ taking into account nonlocal Coulomb screening in a WSe_2 monolayer (light brown hypersurface). The calculated eigenenergies of the 1s and 2p exciton states of −245 meV and −75 meV, respectively, are indicated by red lines. $V_{hydrogen}$ indicates the bare two-dimensional Coulomb potential.

exclusively creates 1*s* excitons, all 1*s* excitons are fully accounted for by the infrared response, and nonlocal screening is essential. Interestingly, the model fit cannot reproduce an additional fine structure discernible at $t_{PP} = 1.6$ ps (Fig. 2e,f) in the energy window between 125 and 165 meV. We suggest that these features may be caused by the formation of trapped excitons or trions, where additional electronic resonances are expected, in analogy with the hydrogen anion[2,10,14,15,22,27] (see Supplementary Section 7).

Figure 3 summarizes the fitting parameters extracted from response functions at different pump fluences Φ and fixed $t_{PP} = 75$ fs (Supplementary Fig. 5). n_X (Fig. 3a, red spheres) agrees perfectly with the density of absorbed pump photons (broken line) and shows no sign of saturation. Remarkably, a slight redshift of E_{res} (Fig. 3b) and a strong increase of the linewidth Δ from 120 to 180 meV (Fig. 3c) is seen with increasing density, even though the maximum value of $n_X = 6.4 \times 10^{12}$ cm^{-2} is still one order of magnitude below the Mott density estimated by close packing of spheres. The broadening of the 1*s*–2*p* transition is possibly dominated by the width of the spatially more extended 2*p* state. This assumption is supported by the relatively narrow PL linewidth of 45 meV. In view of Fig. 3, we attribute the transient blueshift of E_{res} and the decrease of Δ observed in Fig. 2 mainly to the combined effect of the density-driven renormalization of the resonance and the decay of n_X as a function of t_{PP}.

To track the density n_X as a function of t_{PP} more systematically, we record the maximum pump-induced change of the probe field, ΔE_{max}, at fixed $t_{EOS} = 12$ fs (Fig. 1e, red arrow), which is proportional to n_X (see Supplementary Section 10), and scan t_{PP}. For all pump fluences the exciton density sets on rapidly within the duration of the pump pulse of 90 fs (Fig. 4a), and decays subsequently in two distinct steps: a sub-ps dynamics (blue shaded region, Fig. 4a) is followed by a non-exponential decay dominating for $t_{PP} > 0.3$ ps (Fig. 4b).

The latter dynamics is well described by the bi-molecular rate equation $\partial n_X/\partial t = -(\gamma/2)n_X^2$ (Fig. 4b, red solid curves) using the same universal decay constant $\gamma = (0.13 \pm 0.1)$ cm^2 s^{-1} for all pump fluences. This value is comparable to results obtained from interband spectroscopy of other TMDCs (ref. 18). The bi-molecular decay is characteristic of non-radiative Auger recombination[18], whose efficiency is strongly enhanced by the reduced dimensionality and weak screening. Remarkably, subtracting the bi-molecular decay (red solid curves) leaves a subset of excitons (Fig. 4a, blue shaded areas) that decays exponentially (black dashed curves) with a time constant of $\tau = (150 \pm 20)$ fs.

Ultrafast trapping or scattering of excitons cannot cause this extremely fast dynamics because these effects do not change n_X. Also, hypothetical ultrafast non-radiative recombination of excitons can be ruled out as a microscopic origin because such a process would affect all excitons and continue until they are completely annihilated. It would not explain the observed decomposition into two subsets decaying with different dynamics. Because we observe the same relative weight of fast and slow dynamics at all locations of all WSe_2 samples tested, spatial inhomogeneity plays no role either. In contrast, a strong inherent inhomogeneity has been predicted in momentum space[26]: excitons with $K \approx 0$ can couple efficiently with light, whereas large-momentum states are optically dark. The interband dipole moment has been suggested to be sufficiently

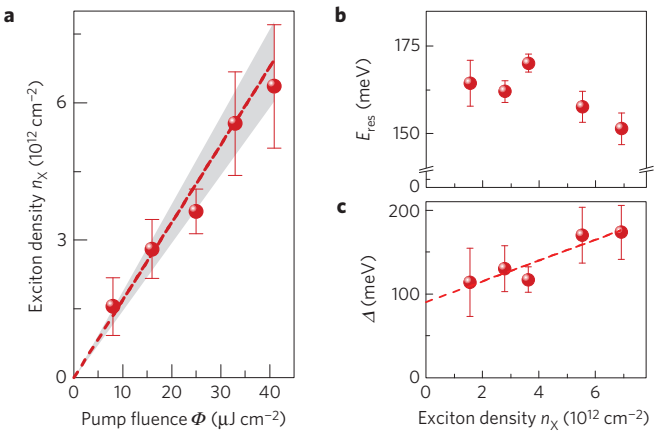

Figure 3 | Density-dependent renormalization of the internal excitonic response. a, 1s-exciton density n_X, as a function of the pump fluence Φ. Red spheres: Values of n_X as extracted by fitting the mid-infrared response functions measured for pump delay time $t_{PP} = 75$ fs (see Fig. 2a,b and Supplementary Fig. 5) with the two-dimensional Wannier model described in the text. Dashed line: Values of n_X as obtained from the pump fluence and the measured absorptivity (Supplementary Information). Grey area: Experimental uncertainty. **b**,**c**, Resonance frequency E_{res} (**b**) and linewidth Δ (**c**) as a function of density n_X. Red spheres: Data extracted by fitting the mid-infrared response functions for $t_{PP} = 75$ fs. Dashed line in **c**: Least-squares linear fit. The error bars represent the 95% confidence intervals of the fitting parameters n_X (**a**), E_{res} (**b**) and Δ (**c**).

large for radiative recombination to become faster than any non-radiative decay—in sharp contrast to the situation in conventional inorganic semiconductors, such as gallium arsenide, where radiative recombination is slower by at least two orders of magnitude. Our experimental data are characteristic of this novel scenario and the time constant τ found above is similar to radiative decay times computed for MoS_2 (ref. 26). This picture is also corroborated by a detailed analysis of the linewidth Δ as a function of t_{pp} (see Supplementary Fig. 6) and a systematic variation of the pump wavelength (see Supplementary Figs 3 and 9).

Once excitons are optically created at $K = 0$ they may either recombine radiatively (Fig. 4c) or scatter with phonons or background carriers into dark states outside the light cone. Large-momentum states are still visible to the probe pulse, but their radiative annihilation is blocked and the fastest remaining decay channel is given by Auger recombination (Fig. 4d). A detailed rate equation model (Supplementary Fig. 8) allows us to determine the momentum scattering rate converting bright into dark particles as $\Gamma = 3.7$ ps^{-1}. This value is consistent with typical exciton mobilities (see Supplementary Section 11) and increases with temperature (Supplementary Fig. 10). The ratios between the scattering rate Γ, the Auger rate γ and the radiative recombination rate τ^{-1} define the ultimate quantum yield achievable in photonic and optoelectronic TMDC devices exploiting radiative interband transitions. For our experiment the quantum yield is ~0.1, but it depends sensitively on the pump wavelength, the pump fluence and the temperature (see Supplementary Section 11).

In conclusion, the observation of resonant internal exciton absorption in a single-layer TMDC allows us to trace both optically

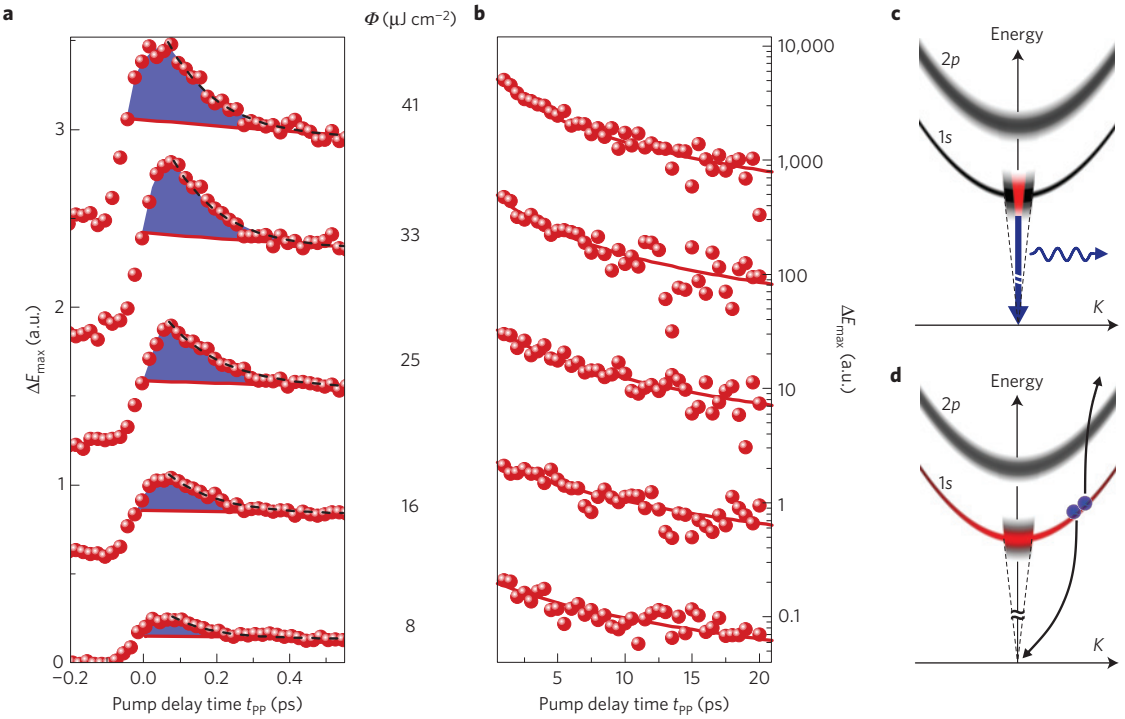

Figure 4 | Ultrafast dynamics of exciton density in single-layer WSe_2. a, The maximum of the pump-induced change ΔE_{max} recorded at a fixed electro-optic sampling time $t_{EOS} = 12$ fs is proportional to the density n_X of 1s excitons (Supplementary Information). ΔE_{max} is shown as a function of the pump delay time $t_{PP} < 0.55$ ps for different fluences Φ (indicated on the right). Curves corresponding to different Φ are vertically offset for better visibility. Red spheres: Experimental data. Red solid curves: Bi-molecular decay model ($\gamma = 0.13$ cm^2 s^{-1}). Blue shaded area: Subset of excitons following an exponential decay ($\tau = 150$ fs). **b**, Semilogarithmic representation of ΔE_{max} as in **a**, for delay times $t_{PP} > 0.55$ ps. **c**, Schematic of the ultrafast radiative interband recombination (blue arrow) of optically bright 1s excitons (red area) at $K \approx 0$ within the light cone (black dashed lines). **d**, Non-radiative exciton annihilation by Auger recombination (black arrows) of a dark population (red area) of excitons (blue spheres) with large centre-of-mass momenta.

dark and bright states. The data quantify internal transition energies, oscillator strengths, densities and many-body effects. These findings represent a qualitatively new benchmark for alternative exciton models[16]. Most remarkably, we reveal the fingerprint of an ultrafast radiative annihilation of 1*s* excitons with vanishing momentum and efficient Auger recombination of dark excitons. The extremely strong coupling of excitons to light opens exciting perspectives for quantum electrodynamics applications[9]. Furthermore, the internal orbital resonances offer a new handle for sophisticated quantum control of monolayer TMDCs.

Methods

Methods and any associated references are available in the online version of the paper.

Received 9 February 2015; accepted 18 June 2015; published online 13 July 2015

References

1. Geim, A. K. & Novoselov, K. S. The rise of graphene. *Nature* **6,** 183–191 (2007).
2. Xia, F., Wang, H., Xiao, D., Dubey, M. & Ramasubramaniam, A. Two-dimensional material nanophotonics. *Nature Photon.* **8,** 899–907 (2014).
3. Wang, Q. H., Kalantar-Zadeh, K., Kis, A., Coleman, J. N. & Strano, M. S. Electronics and optoelectronics of two-dimensional transition metal dichalcogenides. *Nature Nanotech.* **7,** 699–712 (2012).
4. Mak, K. F., Lee, C., Hone, J., Shan, J. & Heinz, T. F. Atomically thin MoS_2: A new direct-gap semiconductor. *Phys. Rev. Lett.* **105,** 136805 (2010).
5. Splendiani, A. *et al.* Emerging Photoluminescence in monolayer MoS_2. *Nano Lett.* **10,** 1271–1275 (2010).
6. Korn, T., Heydrich, S., Hirmer, M., Schmutzler, J. & Schüller, C. Low-temperature photocarrier dynamics in monolayer MoS_2. *Appl. Phys. Lett.* **99,** 102109 (2011).
7. Tonndorf, P. *et al.* Photoluminescence emission and Raman response of monolayer MoS_2, $MoSe_2$, and WSe_2. *Opt. Express* **21,** 4908–4916 (2013).
8. Koppens, F. H. L. *et al.* Photodetectors based on graphene, other two-dimensional materials and hybrid systems. *Nature Nanotech.* **9,** 780–793 (2014).
9. Britnell, L. *et al.* Strong light-matter interactions in heterostructures of atomically thin films. *Science* **340,** 1311–1314 (2013).
10. Mak, K. F. *et al.* Tightly bound trions in monolayer MoS_2. *Nature Mater.* **12,** 207–211 (2013).
11. He, K. *et al.* Tightly bound excitons in monolayer WSe_2. *Phys. Rev. Lett.* **113,** 026803 (2014).
12. Ugeda, M. M. *et al.* Giant bandgap renormalization and excitonic effects in a monolayer transition metal dichalcogenide semiconductor. *Nature Mater.* **13,** 1091–1095 (2014).
13. Chernikov, A. *et al.* Exciton binding energy and nonhydrogenic Rydberg series in monolayer WS_2. *Phys. Rev. Lett.* **113,** 076802 (2014).
14. Ye, Z. *et al.* Probing excitonic dark states in single-layer tungsten disulphide. *Nature* **513,** 214–218 (2014).
15. Berkelbach, T. C., Hybertsen, M. S. & Reichman, D. R. Theory of neutral and charged excitons in monolayer transition metal dichalcogenides. *Phys. Rev. B* **88,** 045318 (2013).
16. Stroucken, T. & Koch, S. W. Optically bright p-excitons indicating strong Coulomb coupling in transition-metal dichalcogenides. Preprint at http://arxiv.org/abs/1404.4238 (2014).
17. Berghäuser, G. & Malic, E. Analytical approach to excitonic properties of MoS_2. *Phys. Rev. B* **89,** 125309 (2014).
18. Kumar, N. *et al.* Exciton–exciton annihilation in $MoSe_2$ monolayers. *Phys. Rev. B* **89,** 125427 (2014).
19. Mak, K. F., He, K., Shan, J. & Heinz, T. F. Control of valley polarization in monolayer MoS_2 by optical helicity. *Nature Nanotech.* **7,** 494–498 (2012).
20. Zeng, H., Dai, J., Yao, W., Xiao, D. & Cui, X. Valley polarization in MoS_2 monolayers by optical pumping. *Nature Nanotech.* **7,** 490–493 (2012).
21. Cao, T. *et al.* Valley-selective circular dichroism of monolayer molybdenum disulphide. *Nature Commun.* **3,** 887 (2012).
22. Jones, A. M. *et al.* Optical generation of excitonic valley coherence in monolayer WSe_2. *Nature Nanotech.* **8,** 634–638 (2013).
23. Yuan, H. *et al.* Generation and electric control of spin–valley-coupled circular photogalvanic current in WSe_2. *Nature Nanotech.* **9,** 851–857 (2014).
24. Kim, J. *et al.* Ultrafast generation of pseudo-magnetic field for valley excitons in WSe_2 monolayers. *Science* **346,** 1205–1208 (2014).
25. Wang, G. *et al.* Gaint enhancement of the optical second-harmonic emission of WSe_2 monolayers by laser excitation at exciton resonances. *Phys. Rev. Lett.* **114,** 097403 (2015).
26. Wang, H. *et al.* Radiative lifetimes of excitons and trions in monolayers of metal dichalcogenide MoS_2. Preprint at http://arxiv.org/abs/1409.3996 (2014).
27. Lui, C. H. *et al.* Trion-induced negative photoconductivity in monolayer MoS_2. *Phys. Rev. Lett.* **113,** 166901 (2014).
28. Kaindl, R. A., Carnahan, M. A., Hägele, D., Lövenich, R. & Chemla, D. S. Ultrafast terahertz probes of transient conducting and insulating phases in an electron–hole gas. *Nature* **423,** 734–738 (2003).
29. Porer, M. *et al.* Non-thermal seperation of electronic and structural orders in a persisting charge density wave. *Nature Mater.* **13,** 857–861 (2014).
30. Castellanos-Gomez, A. *et al.* Deterministic transfer of two-dimensional materials by all-dry viscoelastic stamping. *2D Mater.* **1,** 011002 (2014).

Acknowledgements

We thank M. Eisele, T. Cocker, M. Huber, J. Fabian, A. Chernikov, S. Michaelis de Vasconcellos, R. Schmidt and C. Frankerl for helpful discussions and M. Furthmeier for technical assistance. Support by the European Research Council through ERC grant 305003 (QUANTUMsubCYCLE) and by Deutsche Forschungsgemeinschaft (DFG) through Research Training Group GK1570 and KO3612/1-1 is acknowledged.

Author contributions

C.P., R.B., C.S., T.K. and R.H. planned the project; P.N., G.P., R.B., C.S. and T.K. provided, processed and characterized the samples; C.P., P.S., U.L. and M.P. performed the femtosecond measurements; C.P., P.S., U.L., M.P. and R.H. analysed the data; C.P., P.S. and R.H. elaborated the theoretical model; C.P., P.S. and R.H. wrote the paper with contributions from all authors.

Additional information

Supplementary information is available in the online version of the paper. Reprints and permissions information is available online at www.nature.com/reprints. Correspondence and requests for materials should be addressed to R.H.

Competing financial interests

The authors declare no competing financial interests.

Methods

The investigated system is a monolayer of WSe_2 on a CVD diamond window. Manufactured by mechanical exfoliation and subsequent deterministic transfer[30] from a viscoelastic substrate onto diamond, typical monolayer flakes feature sizes of up to 300 μm × 70 μm. For our experiments, 12-fs light pulses with a centre wavelength of 800 nm are derived from a high-repetition-rate Ti:sapphire amplifier system. A first part of the laser output is filtered by a bandpass with a centre wavelength of 742 nm and a bandwidth of 9 nm, resulting in 90-fs pulses, which selectively inject 1*s* A excitons in the WSe_2 monolayer. Another part of the laser pulses generates few-cycle mid-infrared probe transients through optical rectification in a 50-μm-thick $AgGaS_2$ emitter covering a photon energy range from 125 to 210 meV. The probe pulses are focused onto the sample. The diffraction-limited mid-infrared focal spot (FWHM diameter <35 μm) is set to be distinctly smaller than the area of the monolayer flakes and the optical pump spot, to probe a homogeneously excited sample area. Extending the concept of electro-optic sampling to the mid-infrared spectral range allows us to trace the absolute amplitude and phase of the probe transient, transmitted through the excited and unexcited sample. $\Delta\sigma_1$ and $\Delta\varepsilon_1$ can be extracted independently from each other by a transfer matrix formalism, without resorting to a Kramers–Kronig analysis. In the case of a monolayer this analysis is particularly precise because typical etalon artefacts inside the sample are absent.